

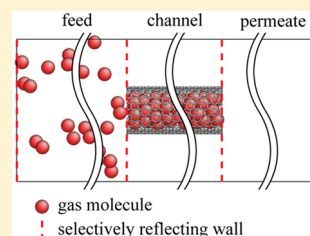
Computational Study of Pressure-Driven Gas Transport in Nanostructured Carbons: An Alternative Approach

Kisung Chae[‡] and Liping Huang^{*}

Department of Materials Science and Engineering, Rensselaer Polytechnic Institute, Troy, New York 12180, United States

ABSTRACT: We demonstrated a computationally efficient method in nonequilibrium molecular dynamics (NEMD) simulations to study pressure-driven gas transport in porous media. The reflecting particle method (RPM)¹⁴ was used to establish a steady-state gas flow along the transport channel, and the gas density in the feed chamber was properly adjusted to allow a constant pressure drop under various conditions by using a perturbation–relaxation loop developed here. This method was validated for methane flow through carbon nanotubes over a wide range of temperatures, giving results comparable to those of the commonly used dual control volume grand canonical molecular dynamics (DCV-GCMD) method but at least 20 times more efficient, even though the transport condition tested is favorable for the latter.

This made it possible to perform systematic studies on the effects of temperature, pressure, and channel size on the transport behaviors. Our study shows that adsorption density varies significantly with temperature, which dramatically influences the transport mechanisms, especially in small channels at low temperatures and under high pressures. This newly developed NEMD method can be readily extended to study gas transport through channels with more complex surface morphology.



1. INTRODUCTION

Pressure-driven gas transport in carbon nanostructures such as amorphous porous carbons (a-PCs) and carbon nanotubes (CNTs) is of significant importance in various fields of science and technologies that include storage,¹ conversion,² and separation.³ Due to the nanostructures' enormous specific surface area and enhanced confinement effect, the interaction between the nanostructured porous carbons and gas molecules in the form of adsorption and surface diffusion is expected to be significant, making the transport behaviors deviate from those in macroscopic channels.⁴ In addition, it has been shown in experiments that the flow of gas and water through CNT composite membranes was greatly enhanced relative to the Knudsen model.^{3,5–7} Even though it is generally believed that the atomic-scale smoothness of the CNT wall is responsible for the enhancement, detailed molecular transport mechanisms remain elusive.

In various molecular dynamics (MD) simulations, transport behaviors of light gases through CNT channels have been extensively studied. For example, both self and transport diffusivities of a wide range of light gases were studied using equilibrium MD (EMD).^{8–12} However, the explicit effect of pressure gradient and the entrance and exit effects cannot be studied directly in EMD. To this end, various nonequilibrium MD (NEMD) methods have been developed. For example, the gravitational method belongs to this category, in which an external dragging force is applied to each atom.¹³ However, this method might suffer from severely disturbed local dynamics.¹⁴ To resolve this, we only applied the external dragging force to atoms within a subset of the system in the local external force (LEF) method.^{15,16} However, even if the external force is exerted in the region away from the transport channel, the effects of artificial force on both local dynamics and transport properties are hard to quantify. The dual control volume grand

canonical MD (DCV-GCMD)^{17,18} is another NEMD technique widely used to study transport, as the gas flow is driven by the pressure difference between the two control volumes, and the entrance and exit effects can be accounted for as well. Unfortunately, this method suffers from the low computational efficiency, mainly due to the fact that the reservoirs need to be constantly refreshed to maintain pressures in the control volumes by adding and removing gas molecules from the system. However, the reflecting particle method (RPM) can be used to generate steady-state pressure-driven flow of gas at a significantly lower computational cost compared to that of the DCV-GCMD method.¹⁴ For example, Bao et al. successfully demonstrated the flow of Ar gas through nanoscale channels by using this method.^{19,20} In addition, water flow through CNTs has also been studied^{21–23} using the RPM.

Despite the computational efficiency of the RPM, the number of molecules in the system needs to be carefully chosen prior to every transport simulation under different conditions with varying pressure (p), temperature (T), and type of gas and channel size. For instance, in an ideal gas limit, the number of gas molecules (N) in the gas chamber varies linearly with p and is inversely proportional to T in the isothermal condition. That is to say,

$$\left(\frac{\partial N}{\partial p}\right)_T \sim T^{-1} \quad (1)$$

Moreover, in a heterogeneous system, the adsorption isotherm of gas would vary significantly with T and p , which will also change N in the gas chamber when the total number of

Received: June 8, 2015

Revised: August 26, 2015

gas molecules in the system is fixed. Therefore, N , under a specific condition, should be evaluated properly in advance to each simulation for a systematic study.

In this study, a perturbation–relaxation loop was added to the RPM to maintain a constant pressure drop between the two gas chambers on the either side of a transport channel. The perturbation–relaxation loop was found to add a marginal computational cost to the RPM, which is desired for a systematic study of the effects of various parameters. Methane permeation through CNTs was studied to validate this alternative NEMD method, and the results were compared with those from other methods and analyzed in detail to illustrate the molecular transport mechanisms. It was found that the adsorption plays a significant role in the transport properties of methane in CNTs, especially in small channels at low temperatures and under high pressures. This newly developed NEMD method can be readily extended to study gas transport through channels with more complex surface morphology, such as in hierarchical nanostructured porous carbons (HNPCs).²⁴

2. COMPUTATIONAL DETAILS

2.1. Reflecting Particle Method. The RPM¹⁴ was used to impose a constant pressure drop (Δp) over the two sides of a transport channel. Specifically, in the RPM there is a fictitious selectively reflecting wall (SRW) acting on the particles on the basis of the direction the particles are crossing the wall; i.e., they are either reflected in a specular manner or remain invisible to the wall. For instance, a particle crossing the SRW from the left to the right would not be hindered, while a particle coming from the right will be reflected with a probability of $1 - P$ (see Figure 1a). It should be noted that the SRW does not influence

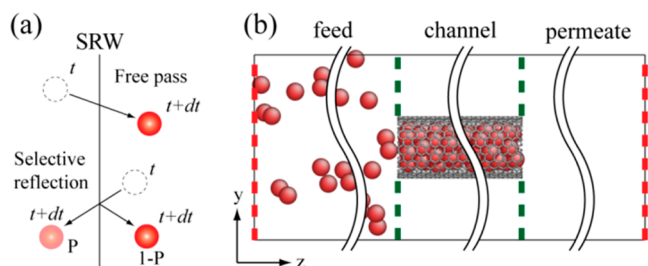


Figure 1. (a) Schematic diagram of the reflecting particle method. (b) A snapshot of the transport simulation with T and p_{feed} values of 200 K and 10 bar, respectively. Locations of SRWs are shown as dashed lines; those marked as red dashed lines are used to generate a gas flow, while those marked as green lines with holes in the middle prevent the gas from flowing outside of the CNT channel (shown in gray). Methane molecules are represented as united atoms in red. The figure was adapted from the original work of Li et al.¹⁴ Note that in the original work, P is the probability of being reflected, while here it is the probability of crossing in this study.

the interactions among gas molecules, and particles across the SRW can still interact with each other. This method has been used to study the steady-state flow of gas and water in previous studies.^{14,20–23} The steady-state permeation was also confirmed in our study by the constant values of feed pressure (p_{feed}), adsorption density, and permeation rate as seen in Figures 2 and 3. The reflection probability can be varied from 0 to 1, affecting both the feed and the permeate chamber pressures. For simplicity, we set the reflection probability at unity for all the conditions, mimicking an evacuation condition in the

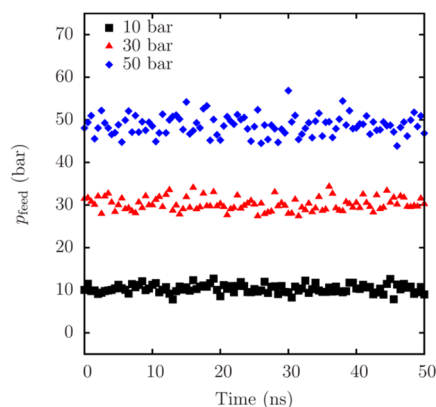


Figure 2. Instantaneous p_{feed} as a function of time, with various p_{target} values indicated in the legend. The system temperature is 600 K in all cases.

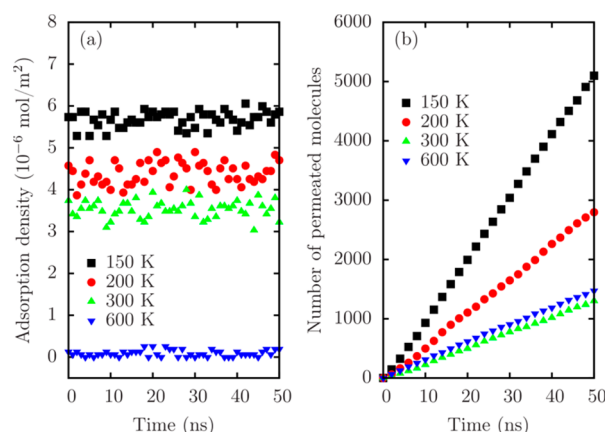


Figure 3. (a) Adsorption density and (b) number of permeated molecules over time at different temperatures.

permeate chamber as seen in Figure 1b. The permeate chamber pressure, therefore, is always close to 0 regardless the choice of T and p (data not shown). The Δp can be written as

$$\Delta p \cong p_{\text{feed}} \quad (2)$$

The RPM was further validated by comparing the transport results with those obtained from the DCV-GCMD and LEF methods. Tests were conducted with methane transport in a (12, 12) CNT of 5 nm in length at various temperatures, and the computational time was measured for 10 ns after the steady-state condition was established. During simulations, carbon atoms in CNT were fixed to save some computational cost. In all of the cases, a chain of 16 Nosé–Hoover (NH) thermostats were used to keep both the global and local temperatures constant, which will be detailed in section 2.2. The CNT was placed in the middle of the simulation box with dimensions of 10 nm \times 10 nm \times 25 nm. Each of the gas chambers was 10 nm in length. In all the cases, the p_{feed} was set at 10 bar, while the permeate chamber was in an evacuation condition. For the DCV-GCMD, 10 attempts at grand canonical Monte Carlo (GCMC) insertion–deletion (without translation) were performed for every MD step in the feed side, giving a MC/MD ratio of 10. However, 100 MC steps were done for every 1000 MD steps in the permeate side. Note that the current choice of MC/MD ratio is quite lenient compared to the 20–100 MC/MD ratios used in the literature^{17,25,15} due

to the low pressures chosen in both chambers. Much higher MC/MD ratios would be required to conduct simulations at higher pressures. However, it should be noted that the computational cost for the RPM would be less sensitive to pressure than the GCMD because there is no adjustable parameter in RPM depending on pressure. Therefore, with low values of p_{feed} , the current transport condition is more favorable for the GCMD. For the LEF method, the permeate chamber was attached with an additional volume inside which the gas molecules were accelerated by the drag force (f_d). The thickness of the additional volume was chosen as 1 nm, and the rest of the setup was similar to those in the other two methods. We varied the magnitude of f_d and the evacuating condition could be achieved at f_d of ~ 0.01 eV/Å. Thus, the transport conditions such as p_{feed} , p_{permeate} , and pressure drop are equivalent to the other two methods at this f_d value. As seen in Figure 4a, the fluxes computed from RPM and DCV-GCMD

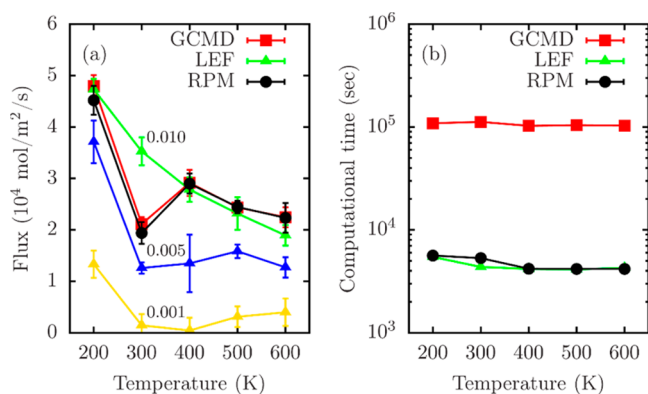


Figure 4. Comparisons of (a) flux and (b) computational time between the RPM, LEF, and DCV-GCMD at various temperatures. For LEF in panel a, the magnitude of drag force (f_d) was marked beside the corresponding curves in units of eV/Å. For panel b, only the data for f_d of 0.01 eV/Å was shown because the computational times were very similar regardless of f_d values.

are almost identical over a wide range of temperatures that we tested. We also confirmed (data not shown) that our DCV-GCMD results are in good agreement with the previous work done by Mutat et al.²⁵ However, transport behavior of the system seems very sensitive to the choice of f_d in the LEF method. For example, the flux at 300 K generated by the LEF is very different from that by the RPM and DCV-GCMD. We confirmed that this comes from the significant difference in the adsorption density throughout the simulation, and the effect of f_d on the local dynamics in the channel is not negligible even if it is applied only in the small portion of the system. Figure 4b shows that the RPM and LEF have similar computational costs and are at least 20 times more efficient than the DCV-GCMD, even though the current transport condition is favorable for the latter.

Despite the computational efficiency, it is difficult to perform a systematic study by using the RPM as discussed previously. To address this issue, we inserted a perturbation–relaxation loop as depicted in Figure 5 to make the p_{feed} consistent with a varying temperature. Each of the iterations is composed of a perturbation process and an equilibration stage. During the perturbation process, the GCMD is performed in the feed chamber, and the number of molecules inside the chamber is varied so that the p_{feed} approaches the target pressure (p_{target}). A

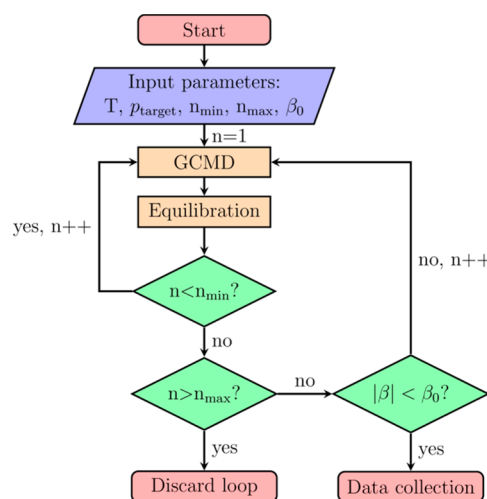


Figure 5. Schematic diagram of the perturbation–relaxation loop to maintain the p_{feed} at a target value.

Metropolis algorithm²⁶ is used to accept or reject each of the insertion and deletion attempts. Translation of the existing molecules was not considered, and any perturbation introduced in the previous procedure is relaxed in the equilibration step so that the system reaches another steady state with the given number of molecules in the system. For instance, if the number of molecules in the feed chamber is increased during the perturbation step, this will increase the p_{feed} temporarily. The increase of the p_{feed} will increase the gas adsorption inside the channel, which may compensate for the excess amount to some extent. During the equilibration step, the p_{feed} is collected at 1 ps intervals to calculate the average feed pressure (\bar{p}). In each loop, the \bar{p} and the p_{target} are compared by means of a relative error (β) as

$$\beta = \frac{\bar{p} - p_{\text{target}}}{p_{\text{target}}} \quad (3)$$

The loop was continued until the magnitude of the relative error is less than a preset criterion, β_0 , which was chosen as 0.05 in this study. The n_{min} and n_{max} are the minimum and maximum numbers of iterations, respectively, for the loop to be performed. Values of 10 and 50 were used for the n_{min} and n_{max} , respectively. The GCMD and equilibration stages were run for 100 and 500 ps, respectively. In the GCMD step, 1000 insertion and deletion attempts were made for every 1000 MD steps to perturb gas in the feed chamber, which gives a MC/MD ratio of 1, high enough so that it can reach the steady state with the desired feed pressure. It should be noted that a significantly smaller MC/MD ratio can be used in comparison to that in the usual range of $10\text{--}10^2$ for transport simulations using the DCV-GCMD technique.^{17,25,15} Thus, the GCMD step in this method is far from time-consuming. For each condition, five parallel samples were generated, each going through an independent loop with a different random seed for the GCMD step. It is shown in Figure 2 that the p_{feed} can be maintained constant at the desired p_{target} value.

2.2. Chain of Nosé–Hoover (NH) Thermostats. In pressure-driven transport simulations, the solid framework is usually held rigid to save some computational cost, and an issue of temperature inhomogeneity would occur as discussed by Newsome and Sholl.²⁷ This is due to the lack of energy exchange between the channel and gas molecules. The gas near

the solid wall is accelerated by the gas–solid interaction, which would cause the local kinetic energy to vary from place to place. Moreover, inhomogeneous density distribution of the gas along the flow direction also has a similar effect due to the gas–gas interaction. As a result, a temperature gradient might develop along the flow direction: higher temperature in the region with higher gas density and vice versa. The use of a global thermostat such as velocity scaling, Berendsen,²⁸ Gaussian, and NH^{29,30} might deteriorate the situation because the equipartition theorem does not hold in the system. A universal velocity scaling parameter calculated from system-wide properties such as kinetic temperature or kinetic energy would solely shift the temperature profile up- or downward. Stochastic thermostats such as Anderson³¹ or Langevin³² would be helpful to eliminate the temperature gradient; however, these methods would have a significant stochastic effect on local dynamics, and transport behaviors would be biased. To address this issue, we divided the simulation box into subsystems with a thin slab geometry along the flow direction. The NH thermostat^{29,30} was then individually applied to each slab. In a chain of NH thermostats, we assumed ergodicity in each subsystem. The chain of thermostats was tested with a setup similar to that used in section 2.1. In this case, the time-averaged local temperature in each bin of 1 nm in thickness was measured for the last 8 ns at a 1 ps interval. The temperature-damping parameter for each NH thermostat was chosen as 0.1 ps. Figure 6 shows the

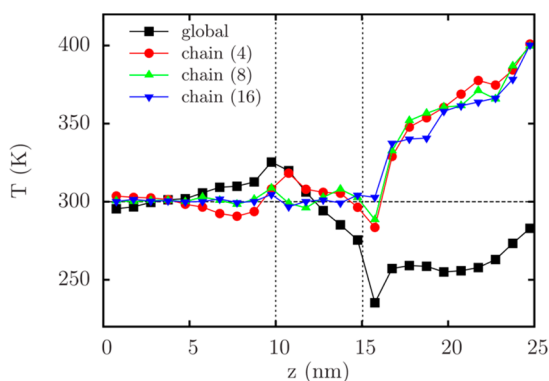


Figure 6. Temperature profiles using the original global NH thermostat and a chain of NH thermostats with different numbers of bins indicated in the legends. The two ends of the transport channel were indicated by dotted lines at 10 and 15 nm, respectively. The temperature was set at 300 K, as indicated by the horizontal dashed line.

temperature profile along the flow direction (z -direction) by using both the original NH thermostat (global) and the chains of thermostats with different number of bins. The temperature gradient within the channel can be clearly seen when the global thermostat was used. The increase of the local temperature near the feed chamber is due to the potential energy decrease of gas molecules as a result of interacting with the solid wall. However, due to the diminished interactions with both the solid wall and other gas molecules, the kinetic energy is lowered near the permeate chamber, giving rise to a significant temperature gradient inside the channel. The chain of thermostats, however, can significantly reduce the temperature gradient within the channel (Figure 6). The increase of local temperature in the permeate chamber seems related to the “flying ice cube” problem³³ because there are few molecules with a finite drift velocity. However, it should be noted that this

region is not important for our transport simulations. Figure 6 shows that the local temperature gets more uniform as the number of bins increases. When 16 bins were used, the system showed a reasonably uniform temperature profile inside the channel region. Further increasing the number of bins will introduce an additional computational cost and a potential disturbance to the local dynamics. Thus, we used a chain of 16 NH thermostats in the rest of our study.

2.3. Details of MD Simulations. In this study, methane was chosen as the permeating gas, which was described by a united atom model. The intermolecular interactions were described by a shifted 12-6 Lennard-Jones (LJ) potential:

$$PE(r) = \phi(r) - \phi(r_c) \quad (4)$$

with

$$\phi(r) = 4\epsilon \left[\left(\frac{\sigma}{r} \right)^{12} - \left(\frac{\sigma}{r} \right)^6 \right] \quad (5)$$

where ϵ and σ are the LJ energy and the size parameter, respectively, and r_c is the cutoff distance (set as 2.5σ in this study). Note that carbon atoms were fixed in their equilibrium positions to save some computational cost. The potential parameters used in this study are as follows: σ_C and ϵ_C/k_B are 0.34 nm and 28 K,³⁴ and σ_{CH_4} and ϵ_{CH_4} are 0.373 nm and 148 K.³⁵ For the interaction between carbon and methane, the Lorentz–Berthelot mixing rule was used.³⁶ To consider the effects of channel size, we used (12, 12) and (25, 25) CNTs with diameters (d_{CNT}) of 1.6 and 3.4 nm, respectively. We did not vary the chirality of the CNTs in our study, as it has been shown that it does not affect the transport of gas molecules.⁸ Temperature was varied in a wide range from 150 to 600 K. It should be noted that the p_{feed} used in this study (10–30 bar) is in the range that the flexibility of CNT does not have a significant effect on transport behaviors.^{9,25,37,38} It has also been shown that the way the methane molecules are modeled has little effect on transport properties in this pressure range.³⁸

We considered any gas molecule as adsorbed if the distance to any of the carbon atoms was less than the adsorption cutoff distance (δ), which was computed as $\sigma_{C-CH_4} + 0.5\sigma_{CH_4}$, i.e., 0.543 nm in this study. A similar approach was previously used by Xi and Shi in studying Ar diffusion in disordered nanoporous carbon.³⁹ Figure 3a shows that a constant adsorption density can be established over a wide range of temperatures with reasonable amount of fluctuations. This confirms that the steady state can be reached by using the perturbation–relaxation loop in the RPM as shown in Figure 5.

Permeation of gas molecules was measured by counting the number of molecules consecutively crossing the two locations across the channel, denoted by l_1 and l_2 , in the feed and the permeate chambers, respectively. Both l_1 and l_2 were placed at a distance δ away from the two ends of the transport channel to count the number of permeations initiated from the gas phase, not from the adsorbed phase. Then, the permeation rate can be computed by taking the slope of the linear fit of the accumulated number of permeated molecules as a function of time as seen in Figure 3b. A constant permeation rate is indicated by the linear increase of the number of permeated molecules with time. Then, the flux along the flow direction (j_z) can be calculated by normalizing the permeation rate by the cross-sectional area of the channel ($0.25 \times \pi \times d_{CNT}^2$). Any

data points in the first 2 ns were discarded to avoid the nonsteady state, if any.

To study detailed transport mechanisms, we measured the passage time (t_{pass}) and number of collisions (n_{col}) for permeated molecules. The t_{pass} value is simply the amount of time for a molecule to pass the two marks (l_1 and l_2). A histogram was generated using all of the measured t_{pass} values of passing molecules. Each of the histograms is normalized to have the area under the curve to be 1. The n_{col} was measured for permeated molecules to count collisions during the passage. Collisions with carbon and other methane molecules were separately measured by using the cutoff of $\sigma_{\text{C-CH}_4}$ and $\sigma_{\text{CH}_4\text{-CH}_4}$, respectively.

3. RESULTS AND DISCUSSION

The adsorption density of methane molecules by varying L_{CNT} , d_{CNT} , and temperature can be seen in Figure 7. L_{CNT} seems to

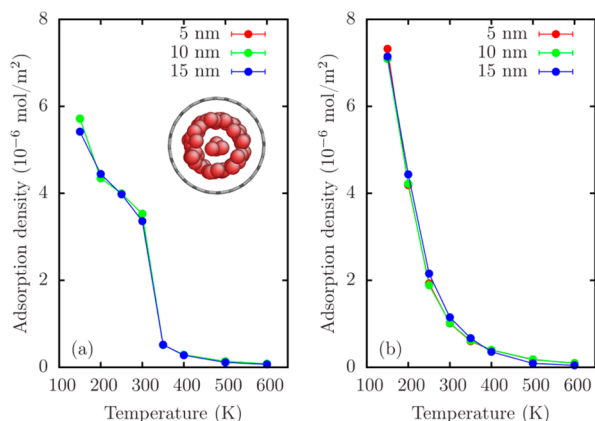


Figure 7. Adsorption density as a function of temperature with different L_{CNT} in (a) (12, 12) and (b) (25, 25) CNTs. Feed pressure was maintained at 10 bar in each case. Adsorption of methane molecules (red balls) can be seen from the top view of the CNT in the inset of (a).

have a negligible effect on adsorption over a wide range of temperature. The adsorptive behavior differs with d_{CNT} at low temperature. In the (25, 25) CNT, the multilayer adsorption seems to take place as temperature is lowered, but it would be hindered for the (12, 12) CNT due to the geometric constraint. In other words, once the monolayer of gas is adsorbed, there is no sufficient room left for the gas adsorption on top of the adsorbed layer due to the small d_{CNT} as can be seen in the inset of Figure 7a. Thus, the increase of adsorption density for the (12, 12) CNT with a decreasing temperature was not as high as for the (25, 25) CNT. The adsorptive behavior with respect to temperature is significantly different depending on the d_{CNT} . In the (12, 12) CNT, the variation of adsorption density with temperature from 150 to 300 K differed significantly from that at temperatures above 350 K, while such a discontinuity was not observed in the (25, 25) CNT. It seems that the high affinity caused by the small channel size as well as the already adsorbed gas molecules is responsible for the abrupt change of the adsorption density.

Figure 8 shows the fluxes of methane through the CNTs with varying L_{CNT} , d_{CNT} , and temperature. Similar to the adsorption density, the flux is insensitive to the L_{CNT} , ranging from 5 to 15 nm in both (12, 12) and (25, 25) CNTs. This may be due to the significantly high interfacial resistance of gas transport (R_{if})

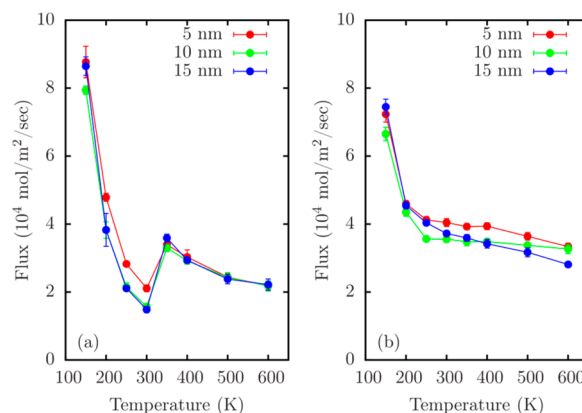


Figure 8. Flux of methane as a function of temperature in (a) (12, 12) and (b) (25, 25) CNT with varying L_{CNT} . Feed pressure was maintained at 10 bar in each case.

compared to the resistance inside of the channel (R_{ch}) as discussed by Newsome and Sholl.⁴⁰ The R_{ch} , which is expected to be proportional to the L_{CNT} , would be very small due to the smooth potential-energy landscape of the CNT. However, the R_{if} would be constant regardless of the L_{CNT} . It was shown that in a (20, 0) CNT, when the L_{CNT} is larger than 3 μm , the R_{if} can be negligible compared to the total permeation resistance, with a transmembrane flux showing a L_{CNT}^{-1} dependency.⁴⁰ Therefore, it is reasonable that the flux is invariant with respect to the L_{CNT} in our study due to the short length of CNTs. Figure 8 also shows that the flux exhibits very different temperature dependence, depending on the d_{CNT} . For example, for the smaller CNT, flux decreases when temperature is increased from 150 to 300 K. This trend is reverted between 300 and 350 K. Then, the flux decreases again with further increase of temperature. This discontinued trend is in agreement with the observation in the adsorptive behavior, and it means that the transport behavior is closely related to the adsorptive behavior. Therefore, the theoretical models developed previously^{41–49} are not applicable to these conditions as adsorption was not taken into account in those models. In contrast, the flux continuously decreases with increasing temperature for the larger CNT. It is interesting to note that over the temperature range from 250 to 400 K, the flux in the larger CNT becomes insensitive to the temperature change. Overall, the flux in the (25, 25) CNT is higher than that in the (12, 12) except at very low temperatures.

The calculated fluxes in this study are on the order of 10^4 mol/m²/sec, in a quantitative agreement with previous MD simulations. Skoulidas et al. reported the flux of methane at room temperature on the order of 10^3 mol/m²/sec in a rigid (10, 10) CNT from EMD.⁸ A Δp value of 1.38 bar was used in their simulation. The flux would further increase to the same order of magnitude as our results when the Δp increases. However, the fluxes measured in experiments are several orders of magnitude smaller than the ones in MD simulations. Usually, when the total area of the membrane is used as the cross-sectional area, the transmembrane fluxes are in the range between 10^{-7} and 10^{-6} mol/m²/sec.^{3,6} Fluxes normalized by the open area of the CNT channel can be obtained by multiplying the transmembrane flux with the porosity of the sample and are on the orders of between 10^{-6} and 10^{-5} mol/m²/sec in CNT membranes with various diameters.^{3,6} This large discrepancy may be partially attributed to the bambooleike

structure and the blockage due to the catalyst particles as prevalently shown in experiments.^{3,50,51} In addition, the CNT area density also influences the transmembrane flux. Yu et al.⁷ reported the transmembrane flux on the order of 10^{-3} mol/m²/sec at the Δp of 10 bar by using the densified CNT membrane with an area density of 2.9×10^{12} cm⁻², which is higher than the area density on the order of 10^{10} cm⁻² used in other experimental studies^{3,5,51} and closer to the value of 4×10^{12} cm⁻² used in the study. Furthermore, the surface morphology of CNT in experiments may deviate from a perfectly graphitic wall. That is, defects on a CNT wall could serve as additional scattering centers to reduce fluxes.

To identify the transport mechanisms under different conditions, we present the distributions of the t_{pass} at different temperatures in Figures 9 and 10 for the (12, 12) and (25, 25)

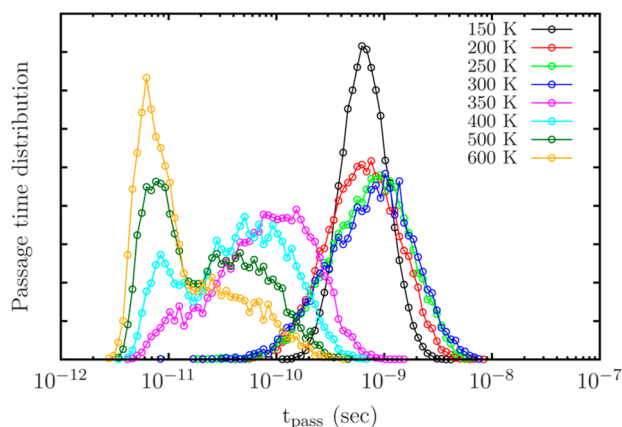


Figure 9. Distribution of the passage time at different temperatures at p_{feed} of 10 bar in the (12, 12) CNT.

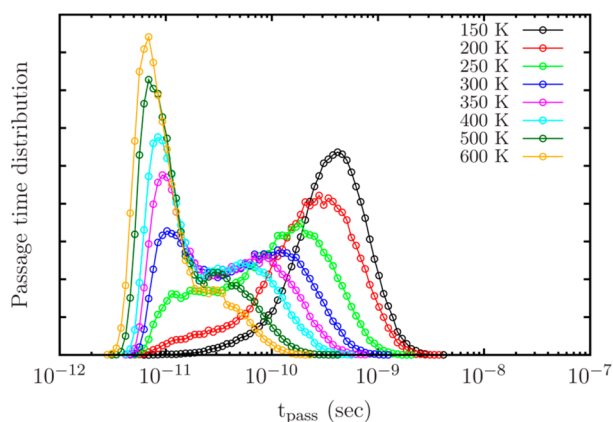


Figure 10. Distribution of the passage time at different temperatures at p_{feed} of 10 bar in the (25, 25) CNT.

CNTs, respectively. Note that the t_{pass} follows a log-normal distribution. It can be seen that the distribution of the t_{pass} changes significantly with temperature. For instance, in the (12, 12) CNT, for temperatures above 400 K, a sharp peak exists for short t_{pass} values around 60 ps, which is comparable to the time needed for gas molecules in the bulk phase to pass the channel at this temperature. Intensity of this peak drops quickly with the decrease of temperature and almost completely disappears at 350 K. When temperature is lower than 300 K, the distribution of the t_{pass} is retarded by over an order of magnitude to form a new peak centered about 800 ps. This

peak is quite broad compared to the high-temperature counterpart, keeping the log scale in mind. We ascribe this to the increased adsorption at temperature below 300 K as seen in Figure 7a. By scrutinizing the trajectory of individual passage events (details included later in this paper), we confirmed that the peak at high temperatures corresponds to the gas–wall collisions, while the peak at low temperatures is mainly due to significant gas–gas collisions near the CNT surface.

However, for the (25, 25) CNT, one can see a gradual transition from the retarded to the fast passage with increasing temperature over the range of temperatures we studied here. At intermediate temperatures ranging from 250 to 400 K, a bimodal distribution is clearly seen, indicating that the two mechanisms occur simultaneously. In other words, some of the gas molecules can pass the channel by colliding dominantly with the wall without much change of momentum, while others are being scattered frequently by other gas molecules. This explains a much broader distribution at low temperatures due to the increased number of gas–gas collisions with the increase of adsorption density.

It is interesting to see that despite the dramatic change of t_{pass} , the flux remains nearly constant from 200 to 400 K in the (25, 25) CNT, as seen in Figure 8b. This temperature range corresponds to the intermediate range where the bimodal distribution is seen (Figure 10). The flux invariance with respect to temperature is due to the following reasons. First of all, despite the shorter average t_{pass} at high temperatures, both the adsorption density and the concentration of gas in the feed chamber are significantly low. However, at low temperatures, even though the average t_{pass} is orders of magnitude longer, the increased adsorption density and gas concentration in the feed chamber make the net flux comparable to that at high temperatures. In other words, at low temperatures, the permeation can be considered as passage-time-limited, while the limiting factor at high temperatures is the concentration. This means that at low temperatures, transport may be controlled by tuning the R_{ch} , which is related to the adsorption density and the surface morphology, while at high temperatures, change of the R_{if} would be more significant.

The scatter plots of the n_{col} and the distribution of the t_{pass} at different temperatures are provided in Figure 11. The number

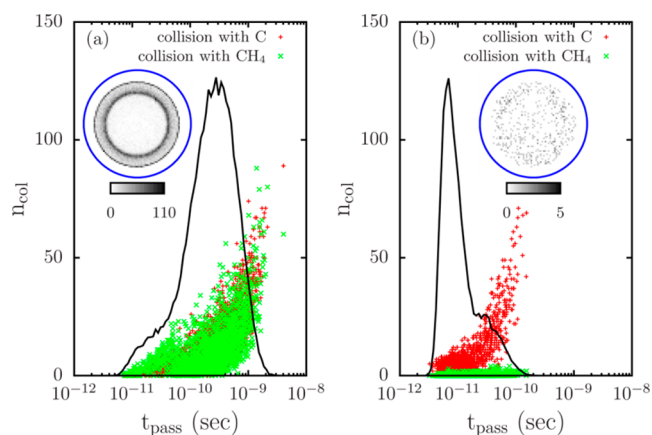


Figure 11. Number of collisions (n_{col}) (red and green symbols) and the passage time distribution (black line) for the (25, 25) CNT at (a) 200 and (b) 600 K. In the insets, gas–gas collision counts are mapped on a cross-section of the CNT in a gray scale. The pixel size was chosen as 0.5 Å. Blue circles indicate the CNT.

of gas–wall collisions and gas–gas collisions are separately shown. It should be pointed out that the gas–wall collision would not change the momentum of permeating gas molecules due to the smooth potential surface of CNTs. In other words, the gas molecules would be mainly reflected by the wall in a specular manner. However, gas–gas collisions would alter the momentum in the flow direction significantly. The inset of Figure 11a shows that such collisions mainly occur near the surface at low temperatures when the adsorption density is high, as seen in Figure 7a. However, when the adsorption density is negligible at 600 K, most of the gas molecules pass the CNT while retaining their initial momentum, which is reflected in the dominant fast peak in the distribution of the t_{pass} . Figure 11a,b shows that it is mainly the gas–gas collisions that give rise to the retarded peak. Low gas–gas collisions and high gas–wall collisions observed at 600 K lead us to believe that the transport mechanism is due to the 2D free-gas diffusion.⁵² This is reasonable because of a low friction force related to the smooth potential energy landscape of CNTs. However, a collective motion of adsorbates near the CNT wall is expected at 200 K due to highly frequent collisions between adsorbed molecules in this region. It is also interesting to see a secondary ring beyond the adsorption layer in Figure 11a, which seems due to the collision with the adsorbed molecules and multilayer formation.

We performed detailed molecular trajectory analysis to verify the transport mechanisms suggested above. For the distributions of the t_{pass} with a bimodal feature at intermediate temperatures ranging from 250 to 400 K, it is shown that the fast peak is due to the permeation of molecules colliding with the wall without significant change of the momenta, as seen in Figure 12a,b. The gas–gas collisions, however, are responsible for the other peak with the longer t_{pass} , as seen in Figure 12c,d. Due to the smooth potential energy landscape of CNTs,⁵² the gas–wall collision is mainly specular. The velocity component of permeating molecules in the flow direction remains unchanged, resulting in the fast transport. However, after gas–gas collisions, gas molecules would lose their momenta in the flow direction during their journey. This explains the retarded passage time as well as their broad distribution as seen in Figures 9 and 10.

In Figure 13, we show the change of fluxes with the p_{feed} value at 200 and 600 K. It is seen that the flux linearly increases with the p_{feed} value. The permeate chamber is evacuated (i.e., $p_{\text{permeate}} \approx 0$), so the Δp value is essentially the p_{feed} value (eq 2). This linear behavior is consistent with many experimental studies on light gas transport through CNT membranes.^{3,6,50,51} Similar to that in experiments, an enhancement of gas transport in CNTs relative to the Knudsen model is observed in our MD simulations (Figure 13), although to a much smaller extent. This is mainly due to the fact that the L_{CNT} in our simulations and the membrane thickness in experiments are quite different (~ 10 nm versus ~ 10 μm). The R_{if} is higher relative to R_{ch} in our CNTs, while the opposite is true in experiments. The discrepancy between the Knudsen model and MD simulations becomes larger with the decrease of temperature, which is due to the higher adsorption density at low temperatures, as seen in Figure 14. The above observations show that at high temperatures, the nature of gas–wall collisions is primarily specular, while at low temperatures, the gas–gas interaction due to enhanced adsorption cannot be ignored. So the Knudsen model, assuming diffuse scattering in the absence of any gas–gas or gas–solid interaction, would not be proper to describe

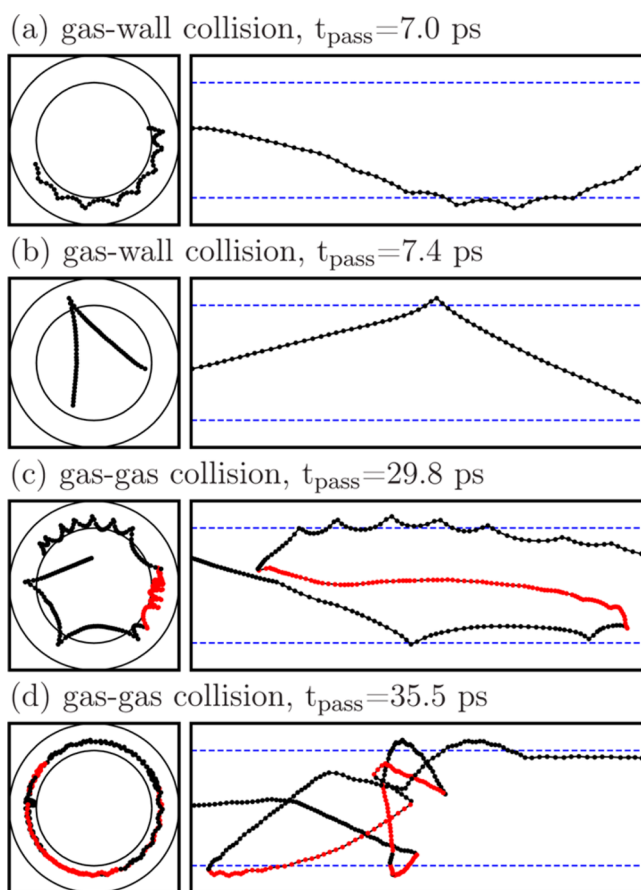


Figure 12. Trajectories of individual passages in the (25, 25) CNT at 400 K, showing the gas–wall collisions (a,b) and gas–gas collisions (c,d). The panels on the left side show the top and side views, respectively. Positions of methane molecules are shown as circles in black and red according to the positive and negative values of v_z , respectively. The radii of inner and outer circles drawn in the left panels correspond to $0.5 \times (d_{\text{CNT}} - \delta)$ and $0.5 \times d_{\text{CNT}}$, respectively, and the region between the two circles indicate the surface adsorption layer. Boundaries of surface adsorption layer are indicated as blue dashed lines in the right panels.

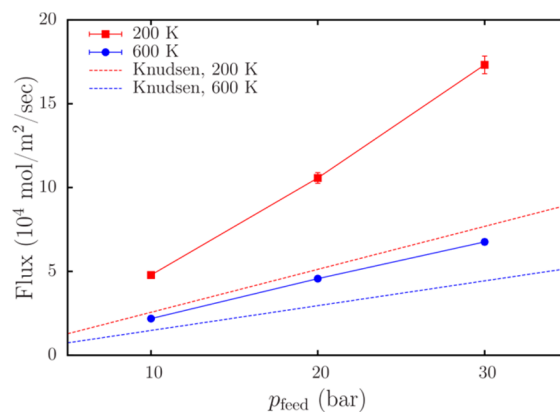


Figure 13. Flux of methane versus the p_{feed} in the (12, 12) CNT with a length of 5 nm. Dashed lines represent fluxes calculated by the Knudsen model.

the gas transport in CNTs, even though the invariant permeance with respect to pressure was observed that can be predicted by the Knudsen model.^{6,53}

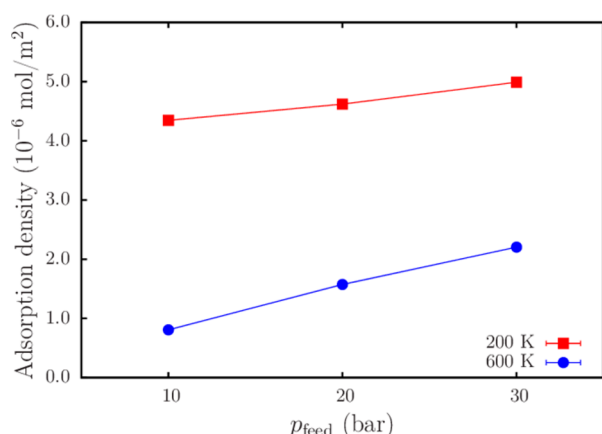


Figure 14. Adsorption density as a function of p_{feed} at 200 and 600 K in the (12, 12) CNT.

In Figure 15, we also show the distributions of t_{pass} in the (12, 12) CNT at 200 and 600 K with different p_{feed} values. At 200 K,

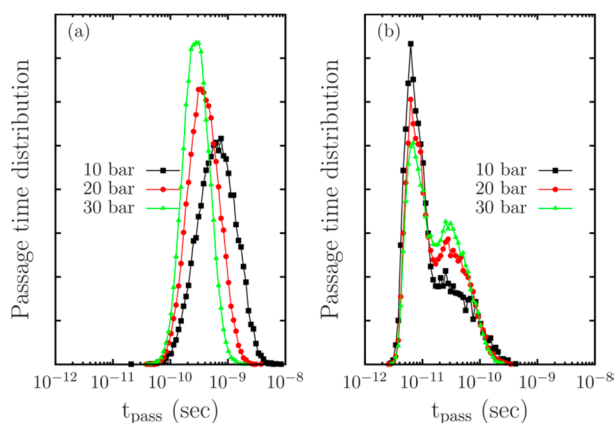


Figure 15. Distribution of the passage time with varying p_{feed} at (a) 200 and (b) 600 K in the (12, 12) CNT.

the t_{pass} is shifted to the shorter values with increasing p_{feed} values. Because a significant amount of adsorption is expected at this temperature (Figure 14), the increased amount of injected gas molecules that possess positive (downstream) momenta to drive the adsorbed phase to move seems to be the cause for the diminished passage time. That is to say, because of the small length of the channels used in this study (5–15 nm), adsorbed molecules are pushed by the injected ones once a monolayer adsorption occurs. However, the peaks of the passage time distribution do not change with the p_{feed} at 600 K, but the amplitude of the fast peak diminishes with increasing p_{feed} , while the retarded peak gains intensity. This is due to the increased interaction between gas molecules with increasing p_{feed} value. In other words, a permeating molecule is more likely to collide with other molecules than with the wall during the passage time when the adsorption density becomes higher and higher (Figure 14). Once again, we show the important role of adsorption in the gas transport mechanisms in CNTs. This would be generally true for gas transport in molecularly confined spaces, especially in narrow channels at low temperatures and high pressures.

4. CONCLUSIONS

In summary, a computationally efficient method in molecular dynamics simulations for the study of pressure-driven gas transport was realized by using the reflecting particle method in conjunction with a perturbation–relaxation loop. This method yields comparable results to those of the dual control volume grand canonical molecular dynamics method, albeit at a much lower computational cost. The transport properties of methane permeating through carbon nanotubes of varying size and length were studied at various pressures and temperatures, and detailed transport mechanisms were also revealed. We showed that adsorption is closely related to transport behaviors, something which has not been taken into account in most of the existing theoretical models. We expect that this computationally efficient method can be easily extended to study transport in more complex nanostructures, especially for a systematic study to separate the effects of many factors on the transport mechanisms.

AUTHOR INFORMATION

Corresponding Author

*Phone: 518-276-2174. Fax: 518-276-8554. E-mail: huangLS@rpi.edu

Present Address

‡Department of Computational Sciences, Korea Institute for Advanced Science, Seoul, 130-722 South Korea.

Notes

The authors declare no competing financial interest.

ACKNOWLEDGMENTS

This work is supported by NSF under grant no. CHE-1012719. Molecular dynamics simulations were performed using LAMMPS⁵⁴ on supercomputers in the Center for Computational Innovations (CCI) at RPI.

REFERENCES

- (1) Sircar, S.; Golden, T. C.; Rao, M. B. Activated Carbon for Gas Separation and Storage. *Carbon* **1996**, *34* (1), 1–12.
- (2) Aricò, A. S.; Bruce, P.; Scrosati, B.; Tarascon, J.-M.; van Schalkwijk, W. Nanostructured Materials for Advanced Energy Conversion and Storage Devices. *Nat. Mater.* **2005**, *4* (5), 366–377.
- (3) Ge, L.; Wang, L.; Du, A.; Hou, M.; Rudolph, V.; Zhu, Z. Vertically-Aligned Carbon Nanotube Membranes for Hydrogen Separation. *RSC Adv.* **2012**, *2* (12), 5329–5336.
- (4) Schoch, R.; Han, J.; Renaud, P. Transport Phenomena in Nanofluidics. *Rev. Mod. Phys.* **2008**, *80* (3), 839–883.
- (5) Holt, J. K. Fast Mass Transport Through Sub-2-Nanometer Carbon Nanotubes. *Science* **2006**, *312* (5776), 1034–1037.
- (6) Zhang, L.; Zhao, B.; Wang, X.; Liang, Y.; Qiu, H.; Zheng, G.; Yang, J. Gas Transport in Vertically-Aligned Carbon Nanotube/parylene Composite Membranes. *Carbon* **2014**, *66*, 11–17.
- (7) Yu, M.; Funke, H. H.; Falconer, J. L.; Noble, R. D. High Density, Vertically-Aligned Carbon Nanotube Membranes. *Nano Lett.* **2009**, *9* (1), 225–229.
- (8) Skoulidas, A.; Ackerman, D.; Johnson, J.; Sholl, D. Rapid Transport of Gases in Carbon Nanotubes. *Phys. Rev. Lett.* **2002**, *89* (18), 185901-1–185901-4.
- (9) Chen, H.; Johnson, J. K.; Sholl, D. S. Transport Diffusion of Gases Is Rapid in Flexible Carbon Nanotubes. *J. Phys. Chem. B* **2006**, *110* (5), 1971–1975.
- (10) Moore, J. D.; Palmer, J. C.; Liu, Y.-C.; Roussel, T. J.; Brennan, J. K.; Gubbins, K. E. Adsorption and Diffusion of Argon Confined in Ordered and Disordered Microporous Carbons. *Appl. Surf. Sci.* **2010**, *256* (17), 5131–5136.

- (11) Palmer, J. C.; Moore, J. D.; Brennan, J. K.; Gubbins, K. E. Adsorption and Diffusion of Argon in Disordered Nanoporous Carbons. *Adsorption* **2011**, *17* (1), 189–199.
- (12) Palmer, J. C.; Gubbins, K. E. Atomistic Models for Disordered Nanoporous Carbons Using Reactive Force Fields. *Microporous Mesoporous Mater.* **2012**, *154*, 24–37.
- (13) Koplik, J.; Banavar, J. R.; Willemsen, J. F. Molecular Dynamics of Fluid Flow at Solid Surfaces. *Phys. Fluids A* **1989**, *1* (5), 781.
- (14) Li, J.; Liao, D.; Yip, S. Coupling Continuum to Molecular-Dynamics Simulation: Reflecting Particle Method and the Field Estimator. *Phys. Rev. E: Stat. Phys., Plasmas, Fluids, Relat. Interdiscip. Top.* **1998**, *57* (6), 7259–7267.
- (15) Arya, G.; Chang, H.-C.; Maginn, E. J. A Critical Comparison of Equilibrium, Non-Equilibrium and Boundary-Driven Molecular Dynamics Techniques for Studying Transport in Microporous Materials. *J. Chem. Phys.* **2001**, *115* (17), 8112.
- (16) Frentrop, H.; Avendaño, C.; Horsch, M.; Salih, A.; Müller, E. A. Transport Diffusivities of Fluids in Nanopores by Non-Equilibrium Molecular Dynamics Simulation. *Mol. Simul.* **2012**, *38* (7), 540–553.
- (17) Heffelfinger, G. S.; van Swol, F. Diffusion in Lennard-Jones Fluids Using Dual Control Volume Grand Canonical Molecular Dynamics Simulation (DCV-GCMD). *J. Chem. Phys.* **1994**, *100* (10), 7548.
- (18) MacElroy, J. M. D. Nonequilibrium Molecular Dynamics Simulation of Diffusion and Flow in Thin Microporous Membranes. *J. Chem. Phys.* **1994**, *101* (6), 5274.
- (19) Bao, F.; Huang, Y.; Zhang, Y.; Lin, J. Investigation of Pressure-Driven Gas Flow in Nanoscale Channels Using Molecular Dynamics Simulation. *Microfluid. Nanofluid.* **2015**, *18* (5–6), 1075–1084.
- (20) Bao, F.; Huang, Y.; Qiu, L.; Lin, J. Applicability of Molecular Dynamics Method to the Pressure-Driven Gas Flow in Finite Length Nano-Scale Slit Pores. *Mol. Phys.* **2015**, *113* (6), 561–569.
- (21) Thomas, J. A.; McGaughey, A. J. H. Reassessing Fast Water Transport Through Carbon Nanotubes. *Nano Lett.* **2008**, *8* (9), 2788–2793.
- (22) Thomas, J.; McGaughey, A. Water Flow in Carbon Nanotubes: Transition to Subcontinuum Transport. *Phys. Rev. Lett.* **2009**, *102* (18), 184502-1–184502-4.
- (23) Thomas, J. A.; McGaughey, A. J. H.; Kuter-Arnebeck, O. Pressure-Driven Water Flow through Carbon Nanotubes: Insights from Molecular Dynamics Simulation. *Int. J. Therm. Sci.* **2010**, *49* (2), 281–289.
- (24) Chae, K.; Shi, Y.; Huang, L. Nanocasting of Hierarchical Nanostructured Porous Carbon in Molecular Dynamics Simulation. *J. Mater. Chem. A* **2013**, *1* (12), 3886–3894.
- (25) Mutat, T.; Adler, J.; Sheintuch, M. Single Species Transport and Self Diffusion in Wide Single-Walled Carbon Nanotubes. *J. Chem. Phys.* **2012**, *136* (23), 234902.
- (26) Metropolis, N.; Rosenbluth, A. W.; Rosenbluth, M. N.; Teller, A. H.; Teller, E. Equation of State Calculations by Fast Computing Machines. *J. Chem. Phys.* **1953**, *21* (6), 1087.
- (27) Newsome, D. A.; Sholl, D. S. Predictive Assessment of Surface Resistances in Zeolite Membranes Using Atomically Detailed Models. *J. Phys. Chem. B* **2005**, *109* (15), 7237–7244.
- (28) Berendsen, H. J. C.; Postma, J. P. M.; van Gunsteren, W. F.; DiNola, A.; Haak, J. R. Molecular Dynamics with Coupling to an External Bath. *J. Chem. Phys.* **1984**, *81* (8), 3684.
- (29) Nosé, S. A Unified Formulation of the Constant Temperature Molecular Dynamics Methods. *J. Chem. Phys.* **1984**, *81* (1), 511.
- (30) Hoover, W. Canonical Dynamics: Equilibrium Phase-Space Distributions. *Phys. Rev. A: At., Mol., Opt. Phys.* **1985**, *31* (3), 1695–1697.
- (31) Andersen, H. C. Molecular Dynamics Simulations at Constant Pressure And/or Temperature. *J. Chem. Phys.* **1980**, *72* (4), 2384.
- (32) Schneider, T.; Stoll, E. Molecular-Dynamics Study of a Three-Dimensional One-Component Model for Distortive Phase Transitions. *Phys. Rev. B: Condens. Matter Mater. Phys.* **1978**, *17* (3), 1302–1322.
- (33) Harvey, S. C.; Tan, R. K.-Z.; Cheatham, T. E. The Flying Ice Cube: Velocity Rescaling in Molecular Dynamics Leads to Violation of Energy Equipartition. *J. Comput. Chem.* **1998**, *19* (7), 726–740.
- (34) Steele, W. A. The Interaction of Rare Gas Atoms with Graphitized Carbon Black. *J. Phys. Chem.* **1978**, *82* (7), 817–821.
- (35) Goodbody, S. J.; Watanabe, K.; MacGowan, D.; Walton, J. P. R. B.; Quirke, N. Molecular Simulation of Methane and Butane in Silicalite. *J. Chem. Soc., Faraday Trans.* **1991**, *87* (13), 1951–1958.
- (36) Allen, M. P.; Tildesley, D. J. *Computer Simulation of Liquids*; Oxford Science Publications; Clarendon Press: Oxford, England, 1989.
- (37) Jakobtorweihen, S.; Verbeek, M. G.; Lowe, C. P.; Keil, F. J.; Smit, B. Understanding the Loading Dependence of Self-Diffusion in Carbon Nanotubes. *Phys. Rev. Lett.* **2005**, *95* (4), 044501-1–044501-4.
- (38) Bartuś, K.; Bródka, A. Methane in Carbon Nanotube: Molecular Dynamics Simulation. *Mol. Phys.* **2011**, *109* (13), 1691–1699.
- (39) Mi, X.; Shi, Y. On the Measurement of Surface Diffusivity in Disordered Nanoporous Carbon via Molecular Dynamics Simulations. *MRS Online Proc. Libr.* **2009**, *16*, 84.
- (40) Newsome, D. A.; Sholl, D. S. Influences of Interfacial Resistances on Gas Transport through Carbon Nanotube Membranes. *Nano Lett.* **2006**, *6* (9), 2150–2153.
- (41) Jepps, O.; Bhatia, S.; Searles, D. Wall Mediated Transport in Confined Spaces: Exact Theory for Low Density. *Phys. Rev. Lett.* **2003**, *91* (12), 126102.
- (42) Jepps, O. G.; Bhatia, S. K.; Searles, D. J. Modeling Molecular Transport in Slit Pores. *J. Chem. Phys.* **2004**, *120* (11), 5396.
- (43) Bhatia, S. K.; Jepps, O.; Nicholson, D. Tractable Molecular Theory of Transport of Lennard-Jones Fluids in Nanopores. *J. Chem. Phys.* **2004**, *120* (9), 4472.
- (44) Bhatia, S. K.; Nicholson, D. Transport of Simple Fluids in Nanopores: Theory and Simulation. *AIChE J.* **2006**, *52* (1), 29–38.
- (45) Arya, G.; Chang, H.-C.; Maginn, E. Knudsen Diffusivity of a Hard Sphere in a Rough Slit Pore. *Phys. Rev. Lett.* **2003**, *91* (2), 026102-1–026102-4.
- (46) Coppens, M.-O.; Froment, G. F. Diffusion and Reaction in a Fractal Catalyst pore—I. Geometrical Aspects. *Chem. Eng. Sci.* **1995**, *50* (6), 1013–1026.
- (47) Coppens, M.-O.; Froment, G. F. Diffusion and Reaction in a Fractal Catalyst pore—II. Diffusion and First-Order Reaction. *Chem. Eng. Sci.* **1995**, *50* (6), 1027–1039.
- (48) Coppens, M.-O.; Froment, G. F. Knudsen Diffusion in Porous Catalysts with a Fractal Internal Surface. *Fractals* **1995**, *3* (4), 807–820.
- (49) Coppens, M. The Effect of Fractal Surface Roughness on Diffusion and Reaction in Porous Catalysts – from Fundamentals to Practical Applications. *Catal. Today* **1999**, *53* (2), 225–243.
- (50) Holt, J. K.; Noy, A.; Huser, T.; Eaglesham, D.; Bakajin, O. Fabrication of a Carbon Nanotube-Embedded Silicon Nitride Membrane for Studies of Nanometer-Scale Mass Transport. *Nano Lett.* **2004**, *4* (11), 2245–2250.
- (51) Kim, S.; Jinschek, J. R.; Chen, H.; Sholl, D. S.; Marand, E. Scalable Fabrication of Carbon Nanotube/Polymer Nanocomposite Membranes for High Flux Gas Transport. *Nano Lett.* **2007**, *7* (9), 2806–2811.
- (52) Verweij, H.; Schillo, M. C.; Li, J. Fast Mass Transport Through Carbon Nanotube Membranes. *Small* **2007**, *3* (12), 1996–2004.
- (53) Kavalenka, M. N.; Striemer, C. C.; Fang, D. Z.; Gaborski, T. R.; McGrath, J. L.; Fauchet, P. M. Ballistic and Non-Ballistic Gas Flow through Ultrathin Nanopores. *Nanotechnology* **2012**, *23* (14), 145706.
- (54) Plimpton, S. Fast Parallel Algorithms for Short-Range Molecular Dynamics. *J. Comput. Phys.* **1995**, *117* (1), 1–19.